Draft version August 28, 2018
Typeset using LaTeX default style in AASTeX62

Contemporaneous X-ray flares in multi-wavelength observations of GRB 140304A at $z = 5.28$

S. Jeong,[1,2] A. J. Castro-Tirado,[2,3] V. Lipunov,[4,5] A. Pozanenko,[6,7] Z. Lucas Uhm,[8,9] I. H. Park,[10] R. Sánchez-Ramírez,[11,2] B. Zhang,[12] B. -B. Zhang,[2,13] D. Xu,[14] N. R. Butler,[15] C. G. Mundell,[16] S. R. Oates,[17] P. Y. Minaev,[6] W. H. Allen,[18] J. Bai,[19] J. Bloom,[20] N. Budnev,[21] A. Claret,[2] A. M. Chernenko,[6] A. Castellón,[22] Ch. Cui,[14] M. D. Caballero-García,[23] R. Cunniffe,[2] S. Castillo-Carrión,[24] F. -K. Peng,[25] R. Fernández-Muñoz,[26] Y. Fan,[19] N. Gehrels,[8] E. Gorbovskoy,[4] J. González,[27] O. Gress,[21] S. Guziy,[28] R. Hudec,[29,30,31] Y. -D. Hu,[2] M. Jelínek,[29] E. V. Klunko,[32] V. Kornilov,[33,5] P. Kubánek,[34] A. Kutyrev,[8] D. Kuvshinov,[33,5] A. Kuznetsov,[4] Kwang H. Lee,[10] William H. Lee,[27] T. de J. Mateo Sanguino,[35] T. Mediavilla,[36] Shashi B. Pandey,[37] C. Pérez del Pulgar,[3] J. Xavier Prochaska,[38] R. Querel,[39] C. G. Román-Zúñiga,[40] E. Ramírez-Ruiz,[38] F. Rendón,[2,41] M. G. Richer,[40] N. Rattenbury,[42] L. Sabau-Graziati,[43] S. E. Schmalz,[44] J. C. Tello,[2] N. Tiurina,[4] N. Tungalag,[45] S. Vitek,[46] V. Vladimirov,[4] A. Volnova,[6] A. M. Watson,[47] Ch. Wang,[19,48] M. Wildi,[49] P. C. M. Yock,[42] and D. Zimnukhov[4]

[1] *Department of Physics, Sungkyunkwan University (SKKU), 2066 Seobu-ro, Suwon, 440 - 746, South Korea*

[2] *Instituto de Astrofísica de Andalucía (IAA-CSIC), Glorieta de la Astronomía s/n, E-18008, Granada, Spain.*

[3] *Departamento de Ingeniería de Sistemas y Automática, Escuela de Ingenierías, Universidad de Málaga, Dr. Pedro Ortiz Ramos, 29071 Málaga, Spain*

[4] *Lomonosov Moscow State University, SAI, 119234 Moscow, Universitetsky pr. 13, Russia*

[5] *Lomonosov Moscow State University, Physics Department, 119991, Moscow, Vorobievy hills, 1, Russia*

[6] *Space Research Institute of the Russian Academy of Sciences, 117997, Profsoyuzanaya, 84/32 Moscow, Russia*

[7] *National Research University Higher School of Economics, Myasnitskaya 20, 101000, Moscow, Russia*

[8] *Astrophysics Science Division, NASA Goddard Space Flight Center, Greenbelt, MD 20771, USA*

[9] *Department of Physics and Astronomy, University of Nevada, Las Vegas, NV 89154, USA*

[10] *Department of Physics, Sungkyunkwan University (SKKU), 2066 Seobu-ro, Suwon, 440-746, South Korea*

[11] *INAF, Istituto Astrofísica de Planetologia Spaziali, Via Fosso del Cavaliere 100, I-00133 Roma, Italy*

[12] *Department of Physics and Astronomy, University of Nevada, Vegas, NV 89154, USA*

[13] *School of Astronomy and Space Science, Nanjing University, Nanjing 210093, China*

[14] *CAS Key Laboratory of Space Astronomy and Technology, National Astronomical Observatories, Chinese Academy of Sciences, Beijing 100101, China*

[15] *School of Earth and Space Exploration, Arizona State University, Tempe, AZ 85287, USA*

[16] *Department of Physics, University of Bath, Claverton Down, Bath, BA2 7AY, UK*

[17] *Department of Physics, University of Warwick, Coventry, CV4 7AL, UK*

[18] *Vintage Lane Observatory, RD3, 7273 Blenheim, New Zealand*

[19] *Yunan Astronomical Observatories, CAS Kunming 650011, Yunnan, China*

[20] *Astronomy Department, University of California, Berkeley, CA 94720-7450, USA*

[21] *Irkutsk State University, Applied Physics Institute, 20, Gagarin blvd, 664003, Irkutsk, Russia*

[22] *Facultad de Ciencias, Universidad de Málaga, Bulevard Louis Pasteur, 29010 Málaga, Spain*

[23] *Astronomical Institute, Academy of Sciences of the Czech Republic, Bocni II 1401, CZ-141 00 Prague, Czech Republic*

[24] *Servicio Central de Informática, Universidad de Málaga, Bulevard Louis Pasteur, 29010 Málga, Spain*

[25] *School of Astronomy and Space Science, Nanjing University, Nanjing 210093, China*

[26] *Instituto de Hortofruticultura Subtropical y Mediterránea La Mayora (IHSM/UMA-CSIC), 29750 Algarrobo Costa, Málaga, Spain*

[27] *Instituto de Astronomía, Universidad Nacional Autónoma de México, Apartado Postal 70-264, 04510 México, D. F., México*

[28] *Nikolaev National University, Nikolska str. 24, 54030 Nikolaev, Ukraine*

[29] *Astronomical Institute, Academy of Sciences of the Czech Republic 251 65 Ondřejov, Czech Republic*

[30] *Department of Radioelectronics, Faculty of Electrical Engineering, Czech Technical University, Technická 2 166 27 Prague, Czech Republic*

[31] *Engelhardt Astronomical observatory, Kazan Federal University, Kremlyovskaya street 18, 420008 Kazan, Russia*

[32] *Institute of Solar-Terrestrial Physics, 664033, p/o box 291, Lermontov st., 126a, Irkutsk, Russia*

[33] *Lomonosov Moscow State University, SAI, 119234 Moscow, Universitetsky pr. 13 Russia*

[34] *Institute of Physics of the Czech Academy of Sciences, Na Slovance, 1999/2, 182 21 Prague 8, Czech Republic*

Corresponding author: I. H. Park
ilpark@skku.edu

[35] Departamento de Ingeniería Electrónica, Sistemas Informáticos y Automática, Universidad de Huelva, 21819 Palos de la Frontera (Huelva), Spain
[36] Scuela Politécnica Superior, Universidad de Cádiz, Avda. Ramon Puyol, 11202 Algeciras (Cádiz), Spain
[37] Aryabhatta Research Institute of Observational Sciences, Manora Peak, Naintial 263129, India
[38] Department of Astronomy and Astrophysics, UCO/Lick Observatory, University of California, 1156 High Street, Santa Cruz, CA 95064, USA
[39] National Institute of Water and Atmospheric Research (NIWA), Lauder, New Zealand
[40] Instituto de Astronomía, Unidad Académica Ensenada, Universidad Autónoma de México, Ensenada BC 22760, México
[41] Estación de Sondeos Atmosféricos (ESAt) de El Arenosillo (CEDEA-INTA), 21130 Mazagón, Huelva, Spain
[42] Department of Physics, University of Auckland, Private Bag 92019, New Zealand
[43] División de Ciencias del Espacio, Instituto Nacional de Técnica Aerospacial (INTA), 28850 Torrejón de Ardoz (Madrid), Spain
[44] Keldysh Institute of Applied Mathematics, Moscow, Russia
[45] Institute of Astronomy and Geophysics, Mongolian Academy of Sciences, Ulaanbaatar, Mongolia
[46] Department of Radioelectronics, Faculty of Electrical Engineering, Czech Technical University, Technická 2 166 27 Prague, Czech Republic
[47] Instituto de Astronomía, Universidad Nacional Autónoma de México, Apartado Postal 70-264, 04510 México, D. F., México
[48] University of Chinese Academy of Sciences, Beijing, 100049, China
[49] Drahtzugstrasse 46, CH-4057 Basel, Switzerland

(Received January 1, 2018; Revised January 7, 2018; Accepted August 28, 2018)

Submitted to ApJ

ABSTRACT

We present multi-wavelength observations of multiple X-ray flares in GRB 140304A, which exploded at redshift $z = 5.283$. Most of X-ray flares in GRBs are observed at early times, but in this case, the cosmological time dilation arising from the high redshift of GRB 140304A helps us catch multiple flares at relatively late times. We show that the combined light curves exhibit at least two pairs of flaring activities in all of gamma-ray, X-ray, and optical bands, which are nearly simultaneous but with some systematic time lags among the peak time of the flares. This temporal association of multiple flares in three different energy bands suggests that the physical mechanism generating the X-ray flares is also responsible for producing the contemporaneous flares in other bands. We examine the nature of these flares in GRB 140304A by investigating the temporal and spectral properties of observations and discuss various implications of our analysis.

Keywords: gamma-ray bursts: general— gamma-ray burst: individual

1. INTRODUCTION

Following the launch of the *Swift* (Gehrels et al. 2004) satellite in 2004, the complex behavior of GRB early X-ray afterglows was discovered (Burrows et al. 2005; O'Brien et al. 2006). Among the surprises were X-ray flares. At least half of the observed GRBs exhibit X-ray flares with light curves, characterized by rapid rises and decays, occurring typically within a few hundreds of seconds after the trigger (Chincarini et al. 2007) and rarely on times scales of ∼1 day or later. These flares, which significantly outshine their afterglow, also exhibit a distinctive pattern of spectral evolution across their rising and falling phases (Falcone et al. 2007). The temporal and spectral morphology implies that such flares likely result from a mechanism occurring during the prompt emission and are, consequently, not explained adequately by a forward external shock model. The steep decay phase of these flares may be dominated by high-latitude emission originating from a bulk-accelerating emission region (Uhm & Zhang 2016a).

As shown by their temporal behaviour (Chincarini et al. 2007; Margutti et al. 2010; Zhang et al. 2014), these flares may originate through a mechanism similar to the one proposed for the prompt emission (Maxham & Zhang 2009) and are possibly a result of the reactivation of the central engine (King et al. 2005; Proga & Zhang 2006). Identification and characterization of prompt emission and early time flares across the electromagnetic spectrum offer a powerful diagnostic of emission mechanisms, shock physics and microphysical properties of the emitting plasma (Lipunov et al. 2016; Gorbovskoy et al. 2016; Troja et al. 2017; Sadovnichy et al. 2018). But obtaining well-sampled multi-wavelength light curves remains technically challenging due to observing constraints, different telescope response speeds, and

rapid temporal variability of flare brightness (characteristic variation timescales δt / t $\ll$ 1). In rare cases, very bright optical counterparts have been detected by small, rapid-response optical telescopes with a wide field of view (Akerlof et al. 1999; Rykoff et al. 2005) or prompt high-energy emission has been unusually long-lived for larger robotic optical telescopes to discover and detect optical emission during part of the high-energy flares (Virgili et al. 2013; Kopac et al. 2015; Mazaeva et al. 2018). But the correlation between optical and high-energy properties has been difficult to establish (Akerlof et al. 2000) or attributed to the reverse component of the external shock (Kobayashi & Sari 2000; Uhm et al. 2012). A brief precursor gamma-ray flash in GRB 160625B acted as an early warning for the main prompt emission event, enabling the first prompt optical polarization measurements and identifying large-scale magnetic fields close to the central engine (Troja et al. 2017). In this paper, we present multi-wavelength observations of GRB 140304A at $z = 5.282$, which show, for the first time, that multiple X-ray flares are observed over five orders in frequency, and flares can be clearly associated with optical re-brightening or "optical flares."

The paper is organized as follows: In Section 2, we discuss the observations and data reductions of GRB 140304A from various telescopes. Section 3 is devoted to analysis of the observed data to understand the properties of GRB 140304A, such as light curves, spectrum analysis, fit of the prompt emission, energy budget in the flares, and so on. In Section 4, we discuss and summarize our main observational findings in GRB 140304A.

2. OBSERVATIONS AND DATA REDUCTIONS

The discovery of GRB 140304A was firstly published by MASTER Global Robotic Net (Gorbovskoy et al. 2014a) and MASTER pointed to the GRB 140304A 84 sec after *Swift* trigger time and detected the optical counterpart of GRB 140304A.

2.1. *Swift/BAT, XRT, UVOT, and Fermi GBM*

On Mar 4, 2014, at 13:22:31UT, GRB 140304A triggered the *Swift* Burst Alert Telescope (BAT). The high energy emission showed a multi-peaked structure with a T_{90} of 15.6 $\pm$ 1.0 s for the 15 - 350 keV band, and the time-averaged spectrum from T - 3.94 to T + 15.77 s is well fit by a simple power law with an index of 1.29 $\pm$ 0.08 (Evans et al. 2014; Marshall & Evans 2014). The narrow-field instrument, X-ray Telescope (XRT) began observation the field, 75.2 s after the BAT trigger, found uncatalogued X-ray source at RA, Dec 30.6412, and 33.4744. The UV/Optical Telescope (UVOT) slewed to observe the field 137 s after the BAT trigger and at the same time, the alert was distributed via the Gamma-ray Coordinate Network (GCN). The UVOT produced a finding chart with an exposure of 250 s with u filter, and no credible afterglow candidate was found in the UVOT FOV (Baumgartner et al. 2014). The UVOT data was checked further at v filter at two flare times, but no significant detections in any image were found due to the high redshift reddening. We extracted the mask-weighted unabsorbed BAT flux density curves at 10 keV with SNR 5 exhibiting bad points, following the standard procedure of the Burst Analyzer[1]. The Burst Analyzer allows us to extract the XRT unobserved flux density light curves and photon index γ as a function of time.

The Fermi Gamma-Ray Burst Monitor triggered and located GRB 140304A (Jenke et al. 2014), which was also detected by *Swift*. The GBM on-ground location is consistent with the *Swift*/XRT location and showed the excess on n5, n3 detectors of GBM. The initial analysis shows that the GBM light curve consists of two main peaks with a combined duration (T_{90}) of 32 $\pm$ 6 s (50 - 300 keV) (Jenke et al. 2014).

2.2. *SPI-ACS*

The Spectrometer for the INTEGRAL (SPI)-AntiCoincidence Shield (ACS) detector (operating in the energy range above $\sim$ 80 keV) onboard the INTErnational Gamma-Ray Astrophysics Laboratory (INTEGRAL) was not triggered by the INTEGRAL Burst Alert System (IBAS) trigger system when the burst occurred. Nevertheless, in the continuous data, a weak but significant emission with duration of 20 s was found. It was corresponding to the prompt emission detected by *Swift*/BAT. The boresight of the burst is 66 degrees. The significance of the measured counts from SPI-ACS was negligible during the flares.

2.3. *MASTER*

[1] http://www.swift.ac.uk/burst_analyser/00590206/

The MASTER Global Robotic Net (Lipunov et al. 2010) responded to GRB 140304A 46 s after the *Swift*/BAT trigger at MASTER-Amur observatory with 10 s exposure and $M_{upperlim}$=13.0 and continued at MASTER-Tunka observatory started 84 s after *Swift*/BAT trigger (Gorbovskoy et al. 2014a,b). All MASTER unfiltered magnitudes were calibrated as 0.2B + 0.8R by the USNO-B1 catalogue (Kornilov et al. 2012). Subsequently, photometric data was processed with Astrokit(Burdanov et al. 2014) in order to minimize the standard deviations among the ensemble of comparison stars, and some stars with significant deviations were removed from the ensemble. Data for both polarizers were processed together, and the output data was cleared of instrumental effects, although some of the average common polarization may remain for the reference stars. Table 1 provides the log of observations and photometry results. The MASTER data of the two polarizers are normalized to the Khureltogot data through comparisons of the detection at 1194 s of MASTER and at 1181 s of Khureltogot.

2.4. *GTC spectral data*

We triggered the Gran Telescopio Canarias to reveal redshift by detecting continuum cutoff for Ly a, and confirmed only redwards of continuum of about 7750 $\AA$ are observed, i.e., the afterglow situated at $z = 5.282$ (Jeong et al. 2014a,b). Optical spectroscopy with OSIRIS at the 10.4 m GTC started on Mar 04, 2014, i.e. $\sim$ 7.36 h after the trigger, using the R2500I VPHs (2 $\times$ 1200 s exposures). The 1.0" slit was positioned on the location of the host galaxy and 2 $\times$ 2 binning mode was used for data acquisition. The obtained spectra were reduced and calibrated following standard procedures using custom tools based in IRAF and Python. The obtained spectra had been flux calibrated using observations of spectro-photometic standard star, HILT600, observed on same night with 2.52 slit. We did slit loss correction on the flux using acquisition image taken with same setup.

2.5. *Khureltogot and Mondy*

We began to observe the optical afterglow of GRB 140304A on March 04 at 13:29:36 UT, i.e., $\sim$ 7 mins later than the *Swift* trigger. The 40 cm ORI-40 telescope of the Khureltogot observatory in Mongolia took 18 unfiltered images with exposures of 60 seconds (Volnova et al. 2014), and an afterglow of the magnitude of 17.8 $\pm$ 0.3 was detected in the first frames. The Khureltogot observatory is also part of the International Scientific Optical Network (ISON, Pozanenko et al. (2013)), and so observations continued at 13:54:10 UT, i.e., $\sim$ 0.5 hr after the burst, with the 1.5 m telescope AZT-33IK of Mondy observatory in Russia (Volnova et al. 2014). We took 43 images in the R-band with exposures of 60 s, and the afterglow was clearly detected in stacked images. We continued observations with the AZT-33IK telescope on March 05 starting at 13:17:34 UT. We took 60 frames with exposures of 120 s using an I-filter, but we did not detect the afterglow in a stacked image. Data were processed using standard routines from the NOAO IRAF software package, CCDPROC (bias, dark reduction, flat field correction), IMAGES (sum and combining) and DAPHOT (point-spread-function, PSF, photometry packages). The photometry is based on reference stars from the SDSS-DR9 data (R mag, transformed from R. Lupton (2005)[2]). The reference stars were selected using an automated on-line procedure for secondary photometric standards identification (Skvortsov et al. 2015). For cross-calibration of the Mondy observations, we added a goodness error for the Mondy data to the GTC sloan-r filter observation as comparing the same reference star.

2.6. *Nanshan*

The 1 m telescope located in Nanshan, Xinjiang, China began observations of GRB 140304A with the R-filter about 21 mins after the trigger and the optical source was clearly detected at the MASTER position (Xu et al. 2014). Nanshans observations were calibrated to the Mondy data by multiplying a normalization factor which is extracted by comparing the flux density at the same observation epoch.

2.7. *BOOTES-4 and all sky camera*

The CASANDRA-4 (Castro-Tirado et al. 2008) all sky camera image obtained at the BOOTES-4 station in Lijiang (China) implies an upper limit for any optical flash simultaneous to the prompt gamma-ray emission of R >7.5.

2.8. *RATIR*

[2] https://www.sdss3.org/dr10/algorithms/sdssUBVRITransform.php

The Reionization and Transients Infrared Camera (RATIR) on the 1.5 m Harold L. Johnson telescope at the Observatorio Astron omico Nacional on Sierra San Pedro M artir in Baja California, Mexico began its observation of the field about 14.4 hr after the BAT trigger. It determined the photometric redshift of z_{phot}=$5.45^{+0.1}_{-0.2}$ (Butler et al. 2014a,b). The RATIR consists of four detectors, two optical and two infrared cameras, allowing four images of a source to be taken simultaneously, either in riZJ or riYH (Fox et al. 2012; Klein et al. 2012; Watson et al. 2012; Butler et al. 2012). The images were reduced in near real-time using a python-based automatic pipeline. Image alignment was conducted with astrometry.net (Lang et al. 2010), and image co-addition was achieved with Astromatic/SWarp (Bertin 2010). We use SExtractor (Bertin & Arnouts 1996) to calculate photometry for individual science frames and mosaics with apertures ranging from 2 to 30 pixels in diameter, with an optical and NIR pixel scales of $0.32''$pixel^{-1} and $0.3''$pixel^{-1}, respectively. Taking a weighted average of the flux in these apertures for all stars in a field, we construct an annular PSF. This point source photometry is then optimized by fitting the PSF to the annular flux values of each source. The r, i and Z -fields are calibrated to the Sloan Digital Sky Survey Data Release 9 (SDSS DR9 (Ahn et al. 2012)). We found that the RATIR and SDSS r, i and Z bands agree to within 3 percent, and the J and H bands are calibrated relative to the Two Micron All Sky Survey (2MASS (Skrutskie et al. 2006)). We use an empirical relation for Y in terms of J and H magnitudes derived from the United Kingdom Infrared Telescope (UKIRT) Wide Field Camera observations (WFCAM (Hodgkin et al. 2009)). The photometric redshift was confirmed also by the Nordic Optical Telescope (NOT, (De Ugarte Postigo et al. 2014)).

3. RESULTS

3.1. *Simultaneous detections of X-ray flares in multi-wavelength bands*

As shown in Figure 1, the observed X-ray light curve shows typical features which have a rapid decay after the prompt emission, a plateau, and more than three subsequent X-ray flares. They are occurring at about 200 s (FX1, 32 s), 600 s (FX2, 114 s), and 1000 s (159 s) in the observer frame (rest frame). MASTER discovered the optical counterpart with a prompt response firstly. MASTER-Amur started observation at 46 s after the trigger and continued in MASTER-Tunka since 84 s. The optical light curve was jointly obtained by a number of different observatories and, specifically, by the MASTER, Khureltogot, Mondy, Nanshan, GTC, RATIR, and BOOTES-4 ground telescopes. Similar to the case of the observed X-ray emission, optical flares following the rapid decay of the early light curve are clearly shown at 400 s (FO1), 800 s (FO2) and, possibly, at 1200 s. Lastly, the gamma ray light curve exhibits at least two flares prior to X-ray flares (See FG1 and FG2).

This is the first time to observe X-ray flares clearly together with optical and gamma-ray regime, and confirms the existence of at least two pairs of "temporal association"among the gamma-ray, X-ray and optical flares. It strongly suggests that the physical mechanism generating these X-ray flares is also responsible for producing the accompanying optical flares. Besides on the two pairs of the early flares, the GRB 140304A shows a late time flare around 25000 s in X-ray and optical regime as shown in Figure 2. The increases in brightness due to the late time flare enables us to find the spectroscopic redshift of GRB 140304A by detections of GTC, and a photometric redshift by RATIR.

Table 1. The log and photometry of optical observations of GRB 140304A. All magnitudes are in the Vega system and they are not corrected to the Galactic extinctions.

2014-03-04T13:23:49.0	82.9	MASTER-II	10	P_{EAST}	16.35 (0.19)
2014-03-04T13:23:55.4	89.3	MASTER-II	10	P_{WEST}	15.98 (0.32)
2014-03-04T13:25:08.3	172.2	MASTER-II	30	P_{EAST}	17.18 (0.17)
2014-03-04T13:25:09.0	172.9	MASTER-II	30	P_{WEST}	17.64 (0.30)
2014-03-04T13:27:00.3	294.2	MASTER-II	50	P_{EAST}	$18.00^{+0.52}_{-0.35}$
2014-03-04T13:27:02.0	295.9	MASTER-II	50	P_{WEST}	$18.41^{+0.81}_{-0.46}$
2014-03-04T13:28:49.8	413.7	MASTER-II	70	P_{EAST}	18.12 (0.29)
2014-03-04T13:30:57.1	556.0	MASTER-II	100	P_{EAST}	18.29 (0.31)

Table 1 continued on next page

Table 1 *(continued)*

2014-03-04T13:30:57.5	556.4	MASTER-II	100	P_{WEST}	$18.39^{+0.52}_{-0.35}$
2014-03-04T13:33:25.9	719.8	MASTER-II	130	P_{EAST}	$18.85^{+0.92}_{-0.49}$
2014-03-04T13:33:26.6	720.5	MASTER-II	130	P_{WEST}	$18.90^{+1.52}_{-0.61}$
2014-03-04T13:36:43.9	937.8	MASTER-II	170	P_{EAST}	18.63 (0.31)
2014-03-04T13:37:09.6	963.5	MASTER-II	170	P_{WEST}	$19.15^{+1.60}_{-0.62}$
2014-03-04T13:40:54.4	1193.3	MASTER-II	180	P_{EAST}	18.63 (0.29)
2014-03-04T13:40:56.1	1195.0	MASTER-II	180	P_{WEST}	$18.72^{+0.54}_{-0.36}$
2014-03-04T13:29:360.0	454.9	Khureltogot(ORI-40)	60	None	17.78 (0.28)
2014-03-04T13:30:410.0	519.9	Khureltogot(ORI-40)	60	None	17.97 (0.22)
2014-03-04T13:31:460.0	584.9	Khureltogot(ORI-40)	60	None	17.94 (0.20)
2014-03-04T13:32:510.0	649.9	Khureltogot(ORI-40)	60	None	18.25 (0.25)
2014-03-04T13:33:560.0	744.9	Khureltogot(ORI-40)	60	None	18.57 (0.26)
2014-03-04T13:36:060.0	874.9	Khureltogot(ORI-40)	60 × 2	None	18.99 (0.24)
2014-03-04T13:38:160.0	974.9	Khureltogot(ORI-40)	60 × 2	None	18.05 (0.24)
2014-03-04T13:39:200.0	1038.9	Khureltogot(ORI-40)	60	None	18.49 (0.28)
2014-03-04T13:40:370.0	1115.9	Khureltogot(ORI-40)	60	None	18.18 (0.28)
2014-03-04T13:41:420.0	1180.9	Khureltogot(ORI-40)	60	None	18.18 (0.20)
2014-03-04T13:42:470.0	1395.9	Khureltogot(ORI-40)	60 × 6	None	18.92 (0.27)
2014-03-04T13:54:10.0	2018.9	Mondy(AZT-33IK)	60 × 4	R	19.97 (0.08)
2014-03-04T13:58:10.0	2258.9	Mondy(AZT-33IK)	60 × 4	R	20.10 (0.09)
2014-03-04T14:02:10.0	2528.9	Mondy(AZT-33IK)	60 ×5	R	20.04 (0.07)
2014-03-04T14:08:10.0	3038.9	Mondy(AZT-33IK)	120 × 5	R	20.19 (0.08)
2014-03-04T14:18:11.0	3639.9	Mondy(AZT-33IK)	120 × 5	R	20.68 (0.13)
2014-03-04T14:28:11.0	4539.9	Mondy(AZT-33IK)	120 × 10	R	20.53 (0.10)
2014-03-04T14:48:12.0	5740.9	Mondy(AZT-33IK)	120 × 10	R	21.07 (0.14)
2014-03-05T13:17:34.0	89705.0	Mondy(AZT-33IK)	120 × 60	I	>19.90
2014-03-04T13:38:00.3	929.26	Nanshan	60	R	19.01 (0.14)
2014-03-04T13:44:26.4	1315.4	Nanshan	60	R	19.40 (0.20)
2014-03-04T13:46:55.5	1464.5	Nanshan	60	R	19.76 (0.27)
2014-03-04T13:49:25.7	1614.7	Nanshan	60	R	19.59 (0.22)
2014-03-04T13:42:46.5	1764.2	Nanshan	60	R	19.52 (0.21)
2014-03-04T14:05:06.4	2555.4	Nanshan	150	R	20.22 (0.26)
2014-03-04T14:16:11.2	3220.2	Nanshan	150	R	20.31 (0.30)
2014-03-04T20:03:26.2	24055.1	GTC	10	i	18.79 (0.04)
2014-03-04T20:05:55.8	24204.7	GTC	10	i	18.74 (0.03)
2014-03-04T20:08:12.5	24341.4	GTC	20	i	18.77 (0.02)
2014-03-04T20:10:50.1	24499.0	GTC	30	i	18.70 (0.03)
2014-03-04T20:26:38.0	25446.9	GTC	60	i	18.77 (0.03)
2014-03-04T20:29:14.3	25603.2	GTC	60	i	18.78 (0.02)
2014-03-04T20:12:12.6	24581.5	GTC	30	r	20.27 (0.03)
2014-03-04T20:24:44.4	25333.4	GTC	60	r	20.26 (0.04)
2014-03-04T20:13:40.5	24669.4	GTC	30	z	17.46 (0.05)

Table 1 continued on next page

Table 1 *(continued)*

2014-03-04T20:22:40.0	25208.9	GTC	60	z	17.49 (0.06)
2014-03-05T03:03:26.0	49254.9	RATIR	1280	r	21.63 (0.13)
2014-03-06T03:06:16.0	135824.9	RATIR	1280	r	22.62 (0.00)
2014-03-05T03:03:26.0	49254.9	RATIR	1280	i	20.28 (0.07)
2014-03-05T03:30:35.6	50884.5	RATIR	1280	i	20.29 (0.08)
2014-03-06T03:06:16.0	135824.9	RATIR	1280	i	22.28 (0.00)
2014-03-05T02:58:40.1	48969.0	RATIR	536.9	z	18.90 (0.06)
2014-03-05T03:25:47.1	50596.0	RATIR	536.9	z	18.94 (0.07)
2014-03-06T03:01:31.1	135540.0	RATIR	536.9	z	20.35 (0.20)
2014-03-04T13:23:57.3	105.5	BOOTES-4	0.5	C	>15.8
2014-03-04T14:18:41.3	3370.3	BOOTES-4	1467.5	C	18.3
2014-03-04T14:14:19.2	3108.2	BOOTES-4	820	g	19.8
2014-03-04T14:18:59.0	3387.9	BOOTES-4	780	r	19.1
2014-03-04T14:28:05.2	4034.2	BOOTES-4	600	i	19.2
2014-03-04T14:32:17.4	4186.4	BOOTES-4	1140	z	19.0

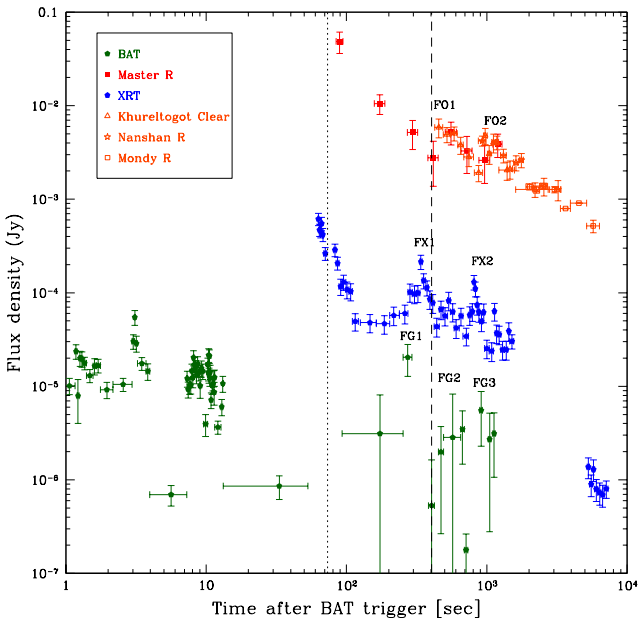

Figure 1. Light curves of GRB 140304A for BAT and XRT observed flux density at 10 keV, and from optical data which were cross-calibrated with the MASTER prompt emission detection and MASTER, Khureltogot, Nanshan, Mondy afterglow data. More than two peaks are apparent (FG1-FX1-FO1 and FG2-FX2-FO2) as flares in the X-ray and optical regimes. In order to view the behavior of the light curves at the three frequencies, we scale the light curves, the optical flux density is multiplied by 50 and BAT flux density is divided by 50. Dotted / dashed lines represent the start times of the first / second BAT LC flares, at 73.2 s and 404 s.

3.2. *Spectral lags between BAT, XRT and optic light curves of the Flare*

Delays in the arrival times of low frequency photons with respect to high frequency photons (called positive spectral lag) in the X-ray flares are observed for GRB 140304A. The light curves in three different bands, gamma-ray, X-ray

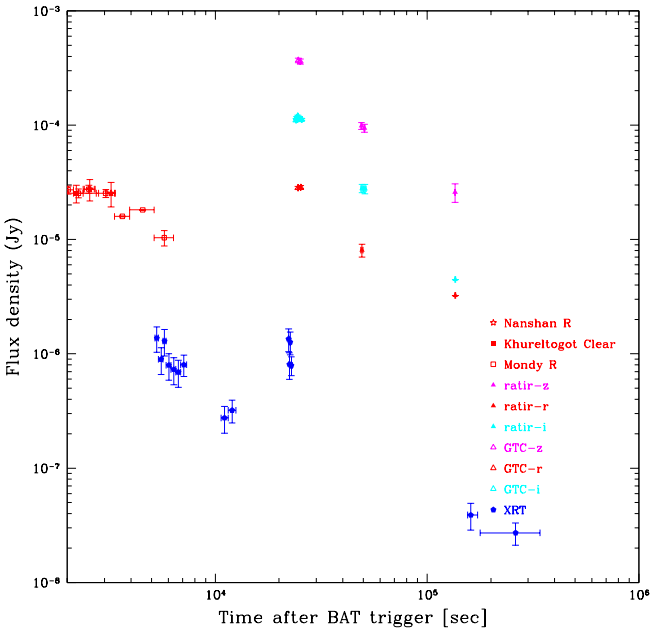

Figure 2. Late time light curves for GRB 140304A from RATIR and the GTC together with those from the Nanshan, Khureltogot and Mondy telescopes for the optical data shown in Figure 1 . X-ray count rates (0.3 - 10 keV) measured with the XRT are also plotted for comparison. GTC optical data were cross-calibrated with data from the MASTER, Khureltogot, Mondy, Nanshan, GTC, and RATIR telescopes. These observations show evidence of a late flare about 25,000 s after the BAT trigger.

and optical bands (presented in Figure 1) clearly indicate the existence of systematic time lags among peak times of the flares.

To investigate the spectral evolution of the flares in terms of spectral lag, we fitted BAT, XRT and optic light curves with a Gaussian function for each flare in the different energy bands individually. Both optical and XRT light curves clearly show two flares while the second flare in BAT data is not statistically significant ($\sim 2\ \sigma$) and during the first flare, there is a gap between 290 s and 380 s in BAT data. We used GAUSSFIT function in IDL with three free parameters (normalization, standard deviation, and peak position of the Gaussian) to obtain the peak positions of the flares and their uncertainties. The dependence of spectral lag on energy is fit by a simple logarithmic function, lag $\sim$ A log(E/1 keV), where E is the geometric mean of the energy of the corresponding energy channel, and A is the spectral lag index (Minaev et al. 2012, 2014). Results of the analysis are presented in Figure 3, where the positions of Gaussian peaks representing each flare in different energy bands are shown. The spectral lag indices of GRB 140304A were found to be $A_1 = 53.2 \pm 2.0$ and $A_2 = 98.4 \pm 8.1$ for the first and the second flare, respectively. One can see in Figure 3 that the gray point, which represents the possible second flare in BAT data, does not contradict the interpolation of the fit obtained for the X-ray and optical data only. This strongly supports the presence of the second flare in the BAT data. The result shows the existence of positive spectral lags for both flares of GRB 140304A over a wide energy range.

To date, this kind of spectral lags has been most frequently observed in the broad pulses in X-ray and gamma-ray range. Under the time stretching of the evolution in GRB 140304A at $z = 5.283$, it allows us to examine X-ray flares in gamma-ray and optical bands together, and suggest that the physical mechanism generating these X-ray flares is also responsible for producing the optical flares.

3.3. *Evolution of Spectral indices during the flares*

We further check the evolution pattern of spectral indices of the flares. As shown in Figure 4, the observed X-ray flares (top panel) exhibit a distinctive pattern of spectral evolution (middle panel): i.e., a hardening of the XRT-band photon index $\hat{\Gamma}$ during the rising phase followed by a softening of the index $\hat{\Gamma}$ during the falling phase. This characteristic behavior is typically observed in X-ray flares. In the bottom panel of Figure 4, we investigated the spectral properties of the flares by measuring, $\beta_{\rm OX}$, determined by fitting a power law from the unabsorbed X-ray flux

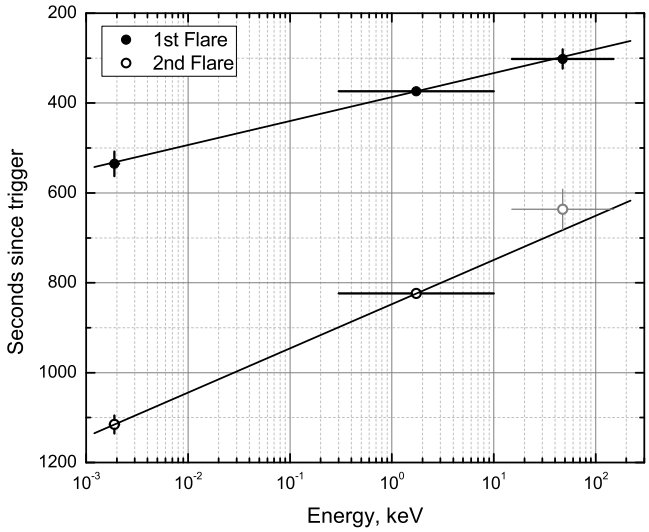

Figure 3. The peak positions of the first (filled circles) and the second (open circles) flare in gamma-, X-ray and optical energy ranges indicate positive spectral lags which can be fitted by a logarithmic function shown by the thick line. The gray point indicates the low significance of the second flare in BAT data. Uncertainties are presented at 1 sigma level.

Table 2. Time-sliced and integrated spectral fits of the prompt emission detected by GBM.

t_1	t_2	CPL				
		Γ_{ph}	E_p	$logNorm$	$\frac{\text{PGSTAT}}{\text{dof}}$	BIC
-2.0	6.5	$-0.85^{+0.17}_{-0.35}$	$138.71^{+105.93}_{-18.37}$	$-0.51^{+0.45}_{-0.25}$	311.3/349	328.92
6.5	15.0	$-0.58^{+0.18}_{-0.44}$	$114.24^{+66.53}_{-10.21}$	$-0.79^{+0.55}_{-0.26}$	287.6/349	305.14
-2.0	15.0	$-0.75^{+0.16}_{-0.30}$	$128.36^{+62.32}_{-12.55}$	$-0.60^{+0.38}_{-0.22}$	312.7/349	330.24

density at 10 keV to the optical flux density at Sloan-r filter, which has a central wavelength of 623 nm. As one can see, the pattern of the $\beta_{\rm OX}$ spectral evolution is identical for each one of the flares during the rising and falling phases. However, we could not study the evolution of the optical spectral index, $\beta_{\rm O}$, due to the lack of observations in filters other than R and r. The behavior of the XRT band photon index, $\hat{\Gamma}$, and $\beta_{\rm X}$ ($=\hat{\Gamma}$-1) are in good agreement with the measured $\beta_{\rm OX}$. The $\beta_{\rm OX}$ values before and after the flares are measured to be 0.79, which is consistent with the values measured for the afterglows and can be explained by the standard afterglow theory (Sari et al. 1998). During the flares, $\beta_{\rm OX}$ varies between 0.1 and 0.5, which indicates that the spectral peak of the $\nu F\nu$ spectrum, i.e., the maximum energy output of the flares, remains within or above the X-ray range. Also, the peak energy output of these flares remains within or below the X-ray range (see Figure 5). Therefore, these flares are indeed the X-ray flares. In terms of the Band function (Band et al. 1993), the measured spectral slope $\beta_{\rm OX}$ (in the range 0.1-0.5 over the duration of the flares) corresponds to a low-energy photon index $\alpha_{\rm B}$ for the Band function in the range between -1.1 and -1.5, which can be naturally explained by the fast-cooling synchrotron mechanism with globally decreasing magnetic fields in the emitting region (Uhm & Zhang 2014).

3.4. *Maximum energy budget of flares on GRB 140304A*

Figure 5 shows the LC at 0.3 - 10 keV (left/top) and 15 - 50 keV (left/middle) from BAT, and >80 keV of the SPI-ACS (left/bottom). The different energy channels are investigated to understand the maximum energy of flares. To check the significance of the flux at each energy channels, a reference point is selected at 73 s, which is the interception point just after the prompt emission and before the X-ray flares. The increase of the flux against time is presented in the Figure 5. The expected first flare regime is 73 s - 400 s, the second is 400 s - 790 s from the Figure 1. The red color indicates 0.3 - 10 keV of BAT, cyan represents 15 - 50 keV of BAT, and green shows >80 keV of the SPI-ACS. The

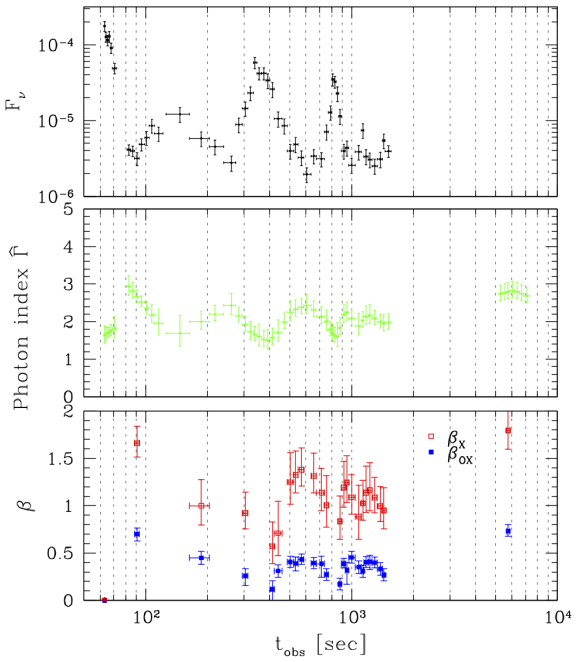

Figure 4. The spectral index of the X-ray to optical bands throughout the duration of the flares. The top panel displayed the X-ray flares observed by the XRT, while the middle panel shows the photon index, $\hat{\Gamma}$ at XRT 10 keV exhibiting characteristics observed in general for X-ray flares: a hardening of the XRT-band photon index $\hat{\Gamma}$ during the rising phase of a flare followed by a softening of the index $\hat{\Gamma}$ during the falling phase. The bottom panel shows the spectral index $\beta_{\rm OX}$ determined by fitting a power law from the unabsorbed X-ray flux density to optical flux density.

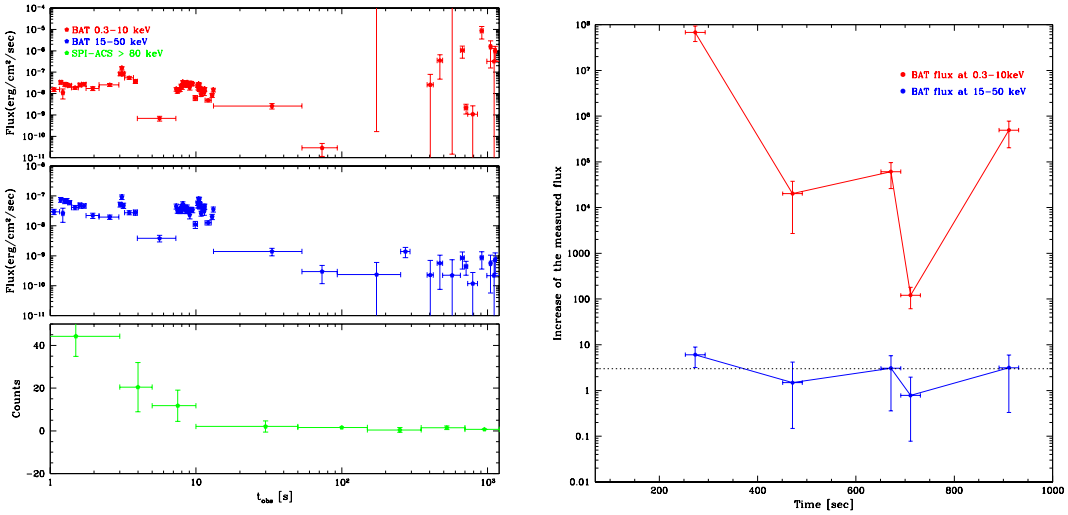

Figure 5. The comparison of detected flares in BAT light curve at 0.3 - 10 keV (left/top), 15 - 50 keV (left/middle), and SPI-ACS (left/bottom). The right figures represents the increase of the measured flux vs time as comparing to the flux at 73 s, which is the time just before starting the flares.

significance of the measured counts from SPI-ACS was negligible during the flares. Even if one considers that the BAT is not sensitive to the photons below 15 keV, the increase on the measured flux at the different energy channels during flaring activity becomes weaker as the energy becomes harder. So the maximum energy during the X-ray flares was

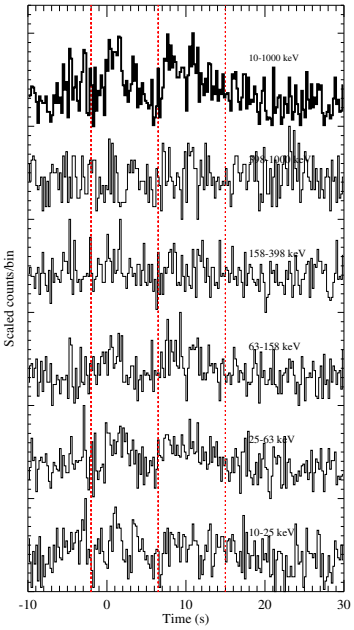

Figure 6. Multi-wavelength light curve of GBM for detector n5.

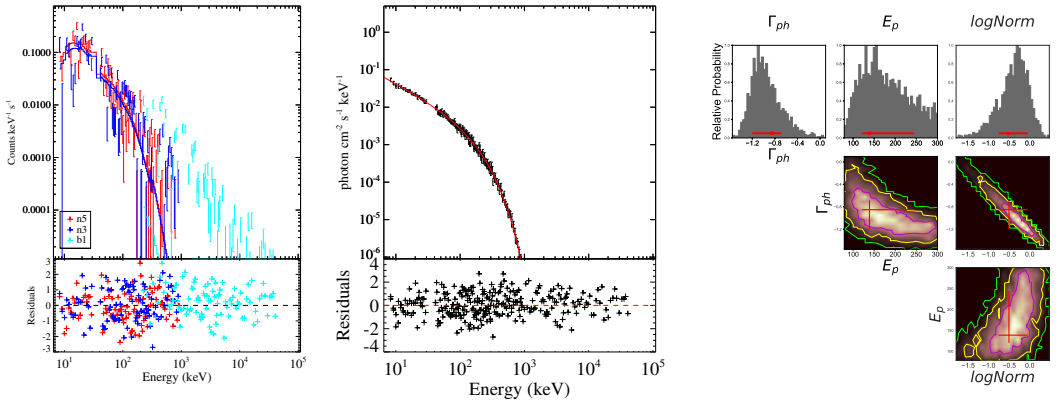

Figure 7. Spectral fitting with CPL for the GBM data at the Interval of -2.0 s and 6.5 s.

well below 50 keV for GRB 140304A, and the dominant energy of the flares resides in 0.3 - 10 keV. And the significance goes weaker as time goes on over the first and second flares.

3.5. *Time-sliced and integrated spectral fits of the prompt emission detected by GBM*

There was no flaring feature shown in *Fermi*/GBM data because GRB 140304A was occulted by Earth during the time when X-ray and optical flares occurred (i.e., 600 s to 3000 s). We however can not rule out the gamma-ray emission of the flares. We only focused on the property of the prompt emission data of GRB 140304A by GBM (see Figure 6). The prompt emissions are divided into 2 slices, between the -2.0 s - 6.5 s and 6.5 s - 15.0 s. The spectra in the first and last slices are well fitted by cutoff power law, with a photon index -0.85 and -0.58, and E_p=139 keV and 114 keV, respectively (see Figure 7). It implies that the mechanism of the prompt emission of GRB 140304A is consistent with synchrotron radiation. The fit results are summarized in Table 2.

3.6. *GTC optical spectrum*

Table 3. EW measurements for the systems detected on the GRB 140304A afterglow spectrum.

Feature	Wavelength	z	EW	eEW
SIIλ1254	7875.5	5.2813	0.23	0.04
SIIλ1260	7913.4	5.2829	0.42	0.01
SiIIλ1260	7919.3	5.2831	0.85	0.03
SiII*λ1265	7945.8	5.2825	1.03	0.03
SiIIλ1304	-	-	-	-
SiII*λ1309	8224.6	5.2818	0.49	0.01
CIIλ1334	8383.5	5.2820	0.86	0.02
CII*λ1336	8390.1	5.2814	0.85	0.02
SiIVλ1394	8755.0	5.2816	0.65	0.04
SiIVλ1403	8812.1	5.2819	0.5	0.05
CIVλ1548	8267.9	4.3403	0.64	0.02
CIVλ1551	8281.6	4.3403	0.5	0.02

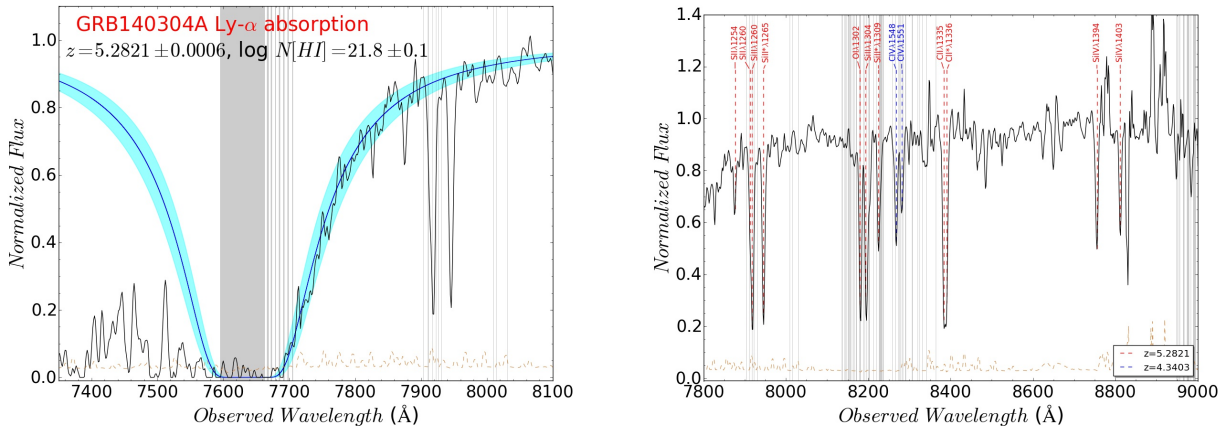

Figure 8. Spectrum and lines detected by the Gran Telescopio Canarias (GTC) on Mar 04, 2014 from GRB 140304A afterglow. The absorbed Lya red damping wing is fit with Voigt profile. The solid cyan area represents the 68 % confidence interval (left).

Besides on the two pairs of the early flares ($> 10^4$ s), the GRB 140304A shows a late time flaring around 25000 s as shown in Figure 2. The increase in luminosity due to the flare enables us to find the spectroscopic redshift of GRB 140304A by triggering the GTC observation. The combined spectrum exhibits the continuum only after 7750Å with a clear discontinuity cut of Lya, which implies that GRB 140304A is a high redshift burst with $z \sim 5$. We fitted the absorbed Lya red damping wing using the Voigt profile and found hydrogen column density as $\log N_{HI} = 21.8 \pm 0.1$(see Figure 8). A series of absorption lines resulting from different species (S, Si, SiII*, OI, C, and CII*) are clearly detected at the same redshift of the Lya feature and confirmed that the afterglow is situated at $z = 5.2821 \pm 0.0006$. Also, at least one intervening CIV system is found at $z = 4.3403 \pm 0.0001$. We excluded the SiIIλ1304 line in this computation, since it looks blended with an unknown intervening feature and no constraint on this component can be imposed in order to perform an accurate de-blending. The earned hydrogen column density is compared with the one of high redshift bursts and GRB damped Lya systems(GRB-DLA), and quasar DLA sample (QSO-DLA) as reported in Figure 9. We chose the QSO-DLA compilation to avoid any false sample in SDSS DLA catalog due to the statistics (Noterdaeme et al. 2012). On the other hand, the compiled sample by Sánchez-Ramírez et al. (2016) takes into account only visually confirmed DLAs, so the distribution is much representative than the actual DLA population. We include in Figure 9 the SDSS sample having $\log N_{HI} \geq 21.7$ DLAs in order to remark the detection of the high column density system, which is very rare towards QSO lines of sight. So the finding of hydrogen column density on the GRB 140304A is a new evidence that GRB and QSO-DLA samples are drawn from

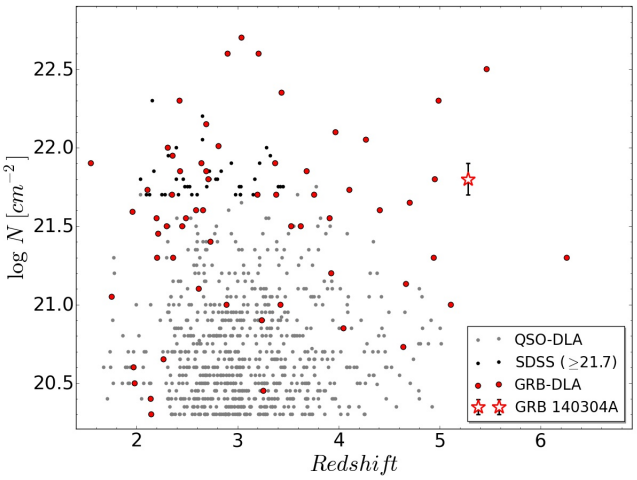

Figure 9. Comparison of the measured column density of the GRB 140304A DLA with the GRB-DLA compilation by Cucchiara et al. (2015) and the QSO-DLA one by Sánchez-Ramírez et al. (2016). QSO-DLA information is complemented with the logN_{HI} ≥21.7 DLAs from the SDSS sample (Noterdaeme et al. 2012). The error bar represents the 68% confidence interval.

different populations. We measured also the equivalent widths (EW) of the lines by fitting with Gaussian profile and computing the sum over the line model. This approximation is valid in low resolution of the GTC/OSIRIS spectrum, as the convolution of the instrumental profile with the actual Voigt profile makes the absorption remain approximately Gaussian. Results are presented in Table 3. This is one of high redshift GRB, which reside larger than $z > 5$, with measured various absorption lines with well defined spectra.

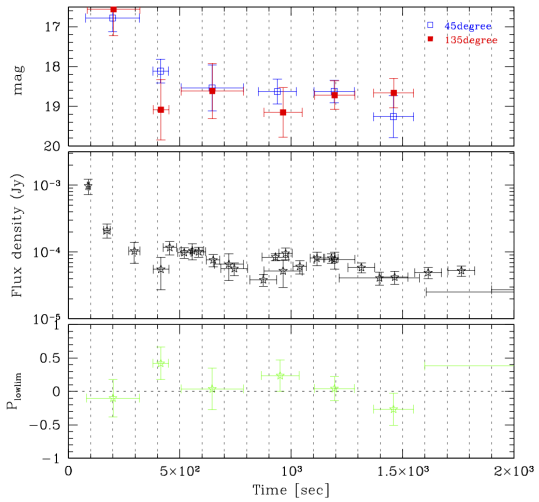

Figure 10. Temporal optical properties of GRB 140304A flare activity measured by the MASTER telescope utilizing two orthogonal linear polarizers

3.7. *Temporal optical properties measured by the MASTER*

We investigated further temporal behavior on the two orthogonal linear polarizers of MASTER telescope during early flares. The top panel in Figure 10 shows the measured counts from each polarizer at 45 degree (I_{45}) and 135 degree (I_{135}), and the middle panel presents the combined optical LC for comparison during flares. The bottom panel shows P_{lowlim}= (I_{45}-I_{135})/(I_{45}+I_{135}). The temporal behavior of the P_{lowlim} suggests some degree of variability before and after the peak of flares, but large uncertainties prevent confirmation at a statistically significant level.

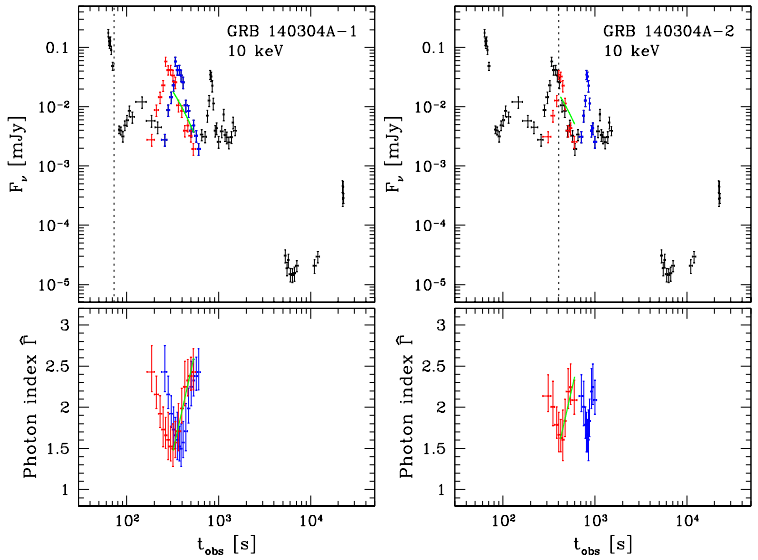

Figure 11. Modeling X-ray flares with a bulk acceleration in the emitting region of GRB 140304A. The result demonstrates that these two X-ray flares are produced while their emitting region is undergoing rapid bulk acceleration

3.8. *Modeling of X-ray flares with the rapid bulk acceleration*

We examine here the first two X-ray flares of GRB 140304A with the theoretical method presented by Uhm & Zhang (2016a) to understand the nature of flare jet. As shown in Figure 11, a proper beginning time t_0 (dotted vertical line) for each X-ray flare is chosen from the gamma-ray light curve (dotted/dashed vertical lines in Figure 1). In the upper left panel, we identify the first flare (blue points) from the XRT light curve (black + blue points) and remove the 't_0-effect' by translating the blue points leftward by the amount $t_0 = 73.2$ s (chosen in Figure 1). The translated X-ray flare (red points) can now be tested against the curvature effect. In the lower left panel, the XRT-band photon indices before and after the translation are correspondingly displayed. By fitting the photon index evolution (green curve in lower left panel), we construct the expected light curve (green curve in the upper left panel), which obeys the standard curvature effect, $\alpha = 2 + \beta$. We can confirm that the decay phase of the first flare of GRB 140304A is steeper than the expected green curve. Then, the generalized version of the high-latitude emission theory (Uhm & Zhang 2015) requires that the emitting region of this flare should undergo rapid bulk acceleration (Uhm & Zhang 2016a; Jia et al. 2016). In the right panels, we repeat these steps for the second X-ray flare with $t_0 = 404$ s and arrive at the same conclusion.

4. DISCUSSIONS AND CONCLUSIONS

In this paper, we focus to discuss the observational properties of GRB 140304A which exploded when the Universe was only 8% of its current age. It shows several flaring activities while it fades out. The time stretching in GRB 140304A helps us to reveal a new behavior on the X-ray flare in multi-wavelength regime. The observation of GRB 140304A was firstly released by MASTER, and we obtained well-sampled optical data during X-ray flares from various ground telescopes. Extensive analysis of the multi-wavelength observations reveals the following properties of GRB 140304A.

1. We find that at least two X-ray flares in GRB 140304A have clear temporal correlations with the flares at optical and gamma-rays. It drew us that the radiation mechanism of the X-ray flares of GRB 140304A governed the optical and gamma-ray emission for GRB 140304A. This is reaffirmed via lag analysis between the peaks of flare over five orders of frequencies that the peaks exhibit the positive spectral lags at least for two pairs of the flares. Recent theoretical study on the X-ray flares reveals that the observed temporal index during the decay phase of X-ray flare is steeper than the expected value, according to the generalized version of the high-latitude emission theory (Uhm & Zhang 2015). It finds out that the emitting region of those flares should undergo rapid bulk acceleration while the flare photons are released to have the observed steep decay (Uhm & Zhang 2016a). Following work presents further the observational evidence of bulk acceleration using large sample of X-ray flares (Jia et al. 2016). We examine here the first two X-ray flares of GRB 140304A with the same theoretical method to understand the nature of flare jet and arrive at the same conclusion that the decay phase of these flares in

GRB 140304A is dominated by the high latitude emission with the rapid bulk acceleration. The physical origin of spectral lags has remained not properly understood despite of rich observational data from the prompt emission broad pulses (Ukwatta et al. 2012; Mochkovitch et al. 2016). Recently, detailed numerical modeling has been performed to reproduce the observed properties of spectral lags in the gamma-ray regime; the model makes use of a simple physical picture that invokes synchrotron radiation originating from a bulk-accelerating emission region (Uhm & Zhang 2016b). However, the physical origin of spectral lags over the wide frequency range needs to be studied further by theoretical modelings to understand the physical nature of the jet.

2. Using the well sampled optical data during flares from the various ground optical telescopes, we confirm the behavior of $\beta_{\rm OX}$ during flares. The measured $\beta_{\rm OX}$ can be naturally explained by the fast-cooling synchrotron mechanism with globally decreasing magnetic fields in the emitting region (Uhm & Zhang 2014). The peak energy output of these flares remains within the X-ray range, as shown by the measured $\beta_{\rm OX}$ values and the spectral analysis for the different energy channels from BAT and SPI-ACS. Due to the lack of optical observations on other filters, $\beta_{\rm O}$ could not be tested to address the possible spectral association between X-ray flares and optical flares.

3. By performing the time-sliced and integrated spectral fits on the prompt emission using *Fermi* GBM data of GRB 140304A, we found that the mechanism of the prompt emission is consistent with synchrotron radiation. This result is in accordance with the possible mechanism of the X-ray flares in GRB 140304A.

4. There are only handful number of GRBs that are observed with a redshift larger than 5. The optical spectrum of GRB 140304A was obtained thanks to the late time flaring activity and shows continuum cutoff of Lya and series of absorption lines, which confirms that the afterglow is located at $z = 5.2821 \pm 0.0006$. The fitted damped feature and earned hydrogen column density gives $\log N_{HI} = 21.8 \pm 0.1$. As in other high redshift GRBs, it places in the context of the GRB-DLA.

5. We further investigate the temporal behaviors in two linear polarizers of MASTER during flares to check any hints on polarizations. The observed brightness is not high enough to prove the polarization at statically significant level. If the flares of GRB 140304A required the bulk acceleration, it provides an important implication on the composition of relativistic jets in GRBs. Since a certain form of additional energy source other than the kinetic energy is demanded to allow for such acceleration, the requirement of bulk acceleration provides a "smoking-gun"evidence that the X-ray flare jets carry a significant Poynting flux in their emitting region. Synchrotron photons emitted from a region with ordered magnetic field lines are expected to be highly polarized. Therefore, one natural consequence of a highly magnetized outflow carried by the X-ray flare jets is then a high degree of polarization since such an outflow originates from the GRB central engine and hence carries some ordered magnetic fields.

X-ray flares are believed to share a similar physical mechanism with the prompt emissions, so the finding of a clear association of optical and X-ray flares in GRB 140304A implies the likelihood that some GRB prompt light curves are accompanied by optical counterparts, as was the case for GRB 080319B (Racusin et al. 2008). Future observatories such as the Ultra-Fast Flash Observatory (UFFO) (Park et al. 2013, 2018; Jeong et al. 2013, 2018; Gaikov & Jeong 2017) which is intended for the detection of the early optical photons during the prompt emission phase, would be able to find more instances of this behavior and quantify the frequency of such associations.

SJ acknowledges the support of the Korea Basic Science Research Program through NRF- 2018R1D1A1B07048993, IHP from National Research Foundation grants of 2018R1A2A1A05022685 and 2017K1A4A3015188. MASTER is supported in parts by Lomonosov Moscow State University Development Program, Moscow Union OPTIKA, and RSF grant 16-12-00085. OG and NB are supported by RFBR grant 17-52-80133. The work was supported in part by agreement with the Russian Federation Ministry of Education and Science (unique identifier RFMEFI59317X0005 / Tunka core facilities). AJCT acknowledges the support from the Spanish Ministry projects AYA 2012-14000-C03-01, AYA 2015-71718R, and the Junta de Andalucía project P12-TIC-2839. AP are partially supported by RFBR grant 17-51-44018. PM and AV acknowledge the support of the RSF grant 18-12-00378. Mondy observations were performed with budgetary funding of Basic Research program II.16 and the data were obtained using the equipment of Center for Common Use "Angara". This work is supported by NASA under an Astrophysics Data Analysis Program (ADAP),

and an Astrophysics Theory Program (ATP) funded to UNLV. This work made use of data supplied by the UK Swift Science Data Centre at the University of Leicester. We thank the RATIR project team and the staff of the Observatorio Astronómico Nacional on Sierra San Pedro Mártir and acknowledge the contribution of Leonid Georgiev to its development. RATIR is a collaboration between the University of California, the Universidad Nacional Autonóma de Mexico, NASA Goddard Space Flight Center, and Arizona State University, benefiting from the loan of an H2RG detector and hardware and software support from Teledyne Scientific and Imaging. RATIR, the automation of the Harold L. Johnson Telescope of the Observatorio Astronómico Nacional on Sierra San Pedro Mártir, and the operation of both are funded through NASA grants NNX09AH71G, NNX09AT02G, NNX10AI27G, and NNX12AE66G, CONACyT grants INFR-2009-01-122785 and CB-2008-101958, NAM PAPIIT grant IG100317, and UC MEXUS-CONACyT grant CN 09-283. SRO gratefully acknowledges the support of the Leverhulme Trust Early Career Fellowship. RS-R acknowledges support from ASI (Italian Space Agency) through the Contract n. 2015-046-R.0 and from European Union Horizon 2020 Programme under the AHEAD project (grant agreement n. 654215). RH acknowledges GACR grant13-33324S. SBP and AP acknowledge BRICS grant number 'DST/IMRCD/BRICS/PilotCall1/ProFCheap/2017(G)' for part of the present work.

REFERENCES

Ahn, C. P., Alexandroff, R., Allende Prieto, C. et al. 2012, ApJS, 203, 21A

Akerlof, C., Balsano, R., Barthelmy, S. et al. 1999, Nature, 398, 400

Akerlof, C., Balsano, R., Barthelmy, S. et al. 2000, ApJ, 532, L25

Band, D., Matteson, J., Ford, L. et al. 1993, ApJ, 413, 28

Baumgartner, W. H., Barthelmy, S. D., Cummings, J. R. et al. 2014, GCNcirc, No.15927

Bertin, E. 2010, ascl.soft,10068B

Bertin, E., Arnouts, S. 1996, A&AS, 117, 393B

Burdanov, A. Y., Krushinsky, V. V., Popov, A. A. 2014, AstBu, 69, 368

Burrows, D. N., Romano, P., Falcone, A. et al. 2005, Science, 309, 1833

Butler, N., Klein, C., Fox, O. et al. 2012, Proc. SPIE, 8446E, 10B

Butler, N., Watson, A. M., Kutyrev, A. et al. 2014, GCNcirc, No. 15928

Butler, N., Watson, A. M., Kutyrev, A. et al. 2014, GCNcirc, No. 15937

Castro-Tirado, A. J., Jelinek, M., Vitek, S. et al. 2008, Proc. SPIE, 70191V, 1

Chincarini, G., Moretti, A., Romano, P. et al. 2007, ApJ, 671, 1903

Cucchiara, A., Fumagalli, M., Rafelski, M. et al. 2015, ApJ, 804, 51

De Ugarte Postigo, A., Gorosabel, J., Xu, D. et al. 2014, GCNcirc, No.15921

Evans, P. A., Beardmore, A. P., Burrows, D. N. et al. 2014, GCNcirc, No.15915

Falcone, A. D., Morris, D., Racusin, J. et al. 2007, ApJ, 671, 1921

Fox, O. D., Kutyrev, A. S., Rapchun, D. A. et al. 2012, Proc. SPIE, 8453E, 1OF

Gaikov, G., Jeong, S., Agaradahalli, V. G. et al. 2017, OptEx, Vol 25, 29143

Gehrels, N., Chincarini, G., Giommi, P. et al. 2004, ApJ, 611, 10051020

Gorbovskoy, E., Lipunov, V., Pruzhinskaya, M. et al. 2014, GCNcirc, No.15914

Gorbovskoy, E., Lipunov, V., Pruzhinskaya, M. et al. 2014, GCNcirc, No.15932

Gorbovskoy, E. S., Lipunov, V. M., Buckley, D. A. H. et al. 2016, MNRAS, 455, 3312

Hodgkin, S. T., Irwin, M. J., Hewett, P. C. et al. 2009, MNRAS, 394, 675H

Jenke, P., Fitzpatrick, G. 2014, GCNcirc, No. 15923

Jeong, S., Nam, J. W., Ahn, K. B. et al. 2013, OptEx, 21, 2263

Jeong, S., Sanchez-Ramirez, R., Castro-Tirado, A. J. et al. 2014, GCNcirc, No. 15922

Jeong, S., Sanchez-Ramirez, R., Gorosabel, J. et al. 2014, GCNcirc, No. 15936

Jeong, S., Panasyuk, M. I., Reglero, V. et al. 2018, SSRv, 214, 16

Jia, L. W., Uhm, Z. L., Zhang, B. 2016, ApJ, 225, 17

King, A., O'Brien, P. T., Goad M. R., et al. 2005, ApJ, 630, 113

Klein, C. R., Kubanek, P., Butler, N. R. et al. 2012, Proc. SPIE, 8453E, 2SK

Kobayashi, S., Sari, R. 2000, ApJ, 542, 819

Kopac, D., Mundell, C. G., Japelj, J. et al. 2015, ApJ, 813, 1

Kornilov, V. G., Lipunov, V. M., Gorbovskoy, E. S. et al. 2012, ExA, 33, 1

Kumar, P. & Zhang, B. 2015, PhR, 561, 1

Laskar, T., Berger, E., Margutti, R. et al. 2018, ApJ, 859, 134
Lang, D., Hogg, D. W., Mierle, K. et al. 2010, AJ, 139, 1782L
Lipunov, V. M., Gorbovskoy, E., Tyurina, N. et al. 2010, AdAst, 349171
Lipunov, V. M., Gorosabel, J., Pruzhinskaya, M. V. et al. 2016, MNRAS, 455, 712
Margutti, R., Guidorzi, C., Chincarini, G. et al. 2010, MNRAS, 406, 2149
Marshall, F. E., Evans, P. A. 2014, GCNcirc, No.15920
Maxham, A. & Zhang, B. 2009, ApJ, 707, 1623
Mazaeva, E., Pozanenko, A., Minaev, P. 2018, IJMPD, 27, 1844012
Minaev, P. Y., Grebenev, S. A., Pozanenko, A. S. et al. 2012, ApJL, 38, 613
Minaev, P. Y., Pozanenko, A. S., Molkov, S. V. et al. 2014, ApJL, 40, 235
Mochkovitch, R., Heussaff, V., Atteia, J. L. et al. 2016, A&A, 592, 95
Norris, J. P., Nemiroff, R. J., Bonnell, J. T. et al. 1996, ApJ, 459, 393
Norris, J. P., Marani, G. F. & Bonnell, J. T. 2000, ApJ, 534, 248
Noterdaeme, P., Petitjean, P., Carithers, W. C. et al. 2012, A&A, 547,1
O'Brien, P. T., Willingale, R., Osborne, J. et al. 2006, ApJ, 647, 1213
Park, I. H., Ahmad, S., Barrillon, P. et al. 2013, NJP 15, 023031
Park, I. H., Panasyuk, M. I., Reglero, V. et al. 2018, SSRv, 214, 14
Pozanenko, A., Elenin, L., Litvinenko, E. et al. 2013, EAS, 61, 259
Proga D., Zhang B. 2006, MNRAS, 370, 61
Racusin, J. L., Karpov, S. V., Sokolowski, M. et al. 2008, Nature455, 183
Rykoff, E. S., Yost, S. A., Krimm, H. A. et al. 2005, ApJ, 631, 121
Sadovnichy, V. A., Panasyuk, M. I., Svertilov, S. I. et al. 2018, ApJ, 861, 48
Sari, R., Piran, T., Narayan R. 1998, ApJ, 497, L17
Skrutskie, M. F., Cutri, R. M., Stiening, R. et al. 2006, AJ, 131, 1163S
Sánchez-Ramírez, R., Ellison, S. L., Prochaska, J. X. et al. 2016, MNRAS, 456, 4488
Skvortsov, N. A., Avvakumova, E. A., Bryukhov, D. O. et al. 2015, AstBu, 71, 114
Troja, E., Lipunov, V. M., Mundell, C. G. et al. 2017, Nature, 547, 425T
Uhm, Z. L, Zhang, B., Hascoët, R. et al. 2012, ApJ, 761, 147
Uhm, Z. L., Zhang, B. 2014, NatPh, 10, 351
Uhm, Z. L., Zhang, B. 2015, ApJ, 808, 33
Uhm, Z. L., Zhang, B. 2016a, ApJ, 824, L16
Uhm, Z. L., Zhang, B. 2016b, ApJ, 825, 97
Ukwatta, T. N., Dhuga, K. S., Stamatikos, M. et al. 2012, MNRAS, 419, 614
Virgili, F. J., Mundell, C. G., Pal'shin, V. et al. 2013, ApJ, 778, 54
Volnova, A., Tungalag, N., Schmalz, S. et al. 2014, GCNcirc, No. 15918
Volnova, A., Pozanenko, A., Korobtsev, I. et al. 2014, GCNcirc, No.15917
Watson, A. M., Richer, M. G., Bloom, J. S. et al. 2012, Proc. SPIE, 8444E, 5LW
Xu, D., Niu, H. B., Feng, G. J. et al. 2014, GCNcirc, No. 15916
Zhang, B. B., Zhang, B., Murase, K. et al. 2014, ApJ, 787, 66